Influence of Preparation and Activation on the Speciation of Carbon-Supported Mo–W Carbides

Parviz Azimov, Céline Sayag, Clement Guibert, Axel Wilson, Abdallah Nassereddine, Antonio Aguilar-Tapia, Jean-Louis F Hazemann, Xavier Carrier

ChemCatChem

ChemCatChem
Chemistry Europe
European Chemical Societies Publishing

RESEARCH ARTICLE OPEN ACCESS

Influence of Preparation and Activation on the Speciation of Carbon-Supported Mo–W Carbides

Parviz Azimov[1] | Céline Sayag[1] | Clement Guibert[1] | Axel Wilson[1] | Abdallah Nassereddine[2] | Antonio Aguilar-Tapia[3] | Jean-Louis Hazemann[2] | Xavier Carrier[1,4]

[1]Laboratoire de Réactivité de Surface, LRS, Sorbonne Université, CNRS, Paris, France | [2]Institut Néel, UPR 2940, CNRS Université Grenoble Alpes, Grenoble, France | [3]Institut de Chimie Moléculaire De Grenoble, UAR2607 CNRS Université Grenoble Alpes, Grenoble, France | [4]Laboratoire Interfaces et Systèmes Electrochimiques, LISE, Sorbonne Université, CNRS, Paris, France

Correspondence: Xavier Carrier (xavier.carrier@sorbonne-universite.fr)

Received: 5 January 2026 | **Revised:** 3 February 2026 | **Accepted:** 6 February 2026

Keywords: carburization mechanism | catalyst synthesis | chemometric analysis | in situ x-ray absorption spectroscopy | Mo–W carbides

ABSTRACT

Carbon-supported Mo–W carbides were synthesized by two different methods (co-impregnation and sequential impregnation of W and Mo precursors) to unravel how precursor impregnation controls carburization pathways. In situ W L_3-edge HERFD-XAS and Mo K-edge XAS, quantitatively analyzed by MCR-ALS reveals that all samples follow a 3-component sequence "oxide → reduced oxide → carbide" upon temperature-programmed carburization. However, the temperature window of the reduced MoO_2–WO_{3-x} coexistence is route-dependent. Co-impregnation and preliminary carburization of W generate extended overlapping domains (300°C-420°C) in which both reduced oxides are simultaneously formed, promoting cooperative oxide-oxide transformations and leading to mixed Mo–W carbidic environments, consistent with XRD and TEM. In contrast, in the route where Mo is carburized first, pre-reduced molybdenum domains trigger early W reduction and shorten the MoO_2–WO_{3-x} overlap window, leading to independent transformation paths for the two metal precursors and to the formation of separate Mo-rich and W-rich carbide phases. These results demonstrate that impregnation and carburization orders are decisive synthetic levers for directing the speciation of Mo–W carbide towards mixed bicarbides or phase-segregated Mo-rich/W-rich carbides providing actionable guidelines for designing bifunctional carbide catalysts.

1 | Introduction

Since the pioneering discovery by Levy and Boudart, who demonstrated the similarities in Pt and W carbide electronic structures, transition metal carbides (TMCs) like molybdenum (Mo) and tungsten (W) carbides have emerged as promising alternatives to noble metals in heterogeneous catalysis [1, 2]. Since then, supported Mo and W carbides have been widely applied in a variety of catalytic reactions including isomerization, hydrogenation, hydrodesulfurization (HDS), hydrodeoxygenation (HDO), biomass conversion and electrocatalysis [3–9]. The growing interest in Mo and W carbides comes not only from their economic advantages and large availability but also from their tolerance to poisoning agents, which frequently deactivate noble metal catalysts [10] making supported carbides particularly attractive for use in harsh catalytic environments.

Beyond their stability, Mo and W carbides exhibit catalytic activities comparable to noble metals, while offering distinct selectivity patterns [11, 12]. Importantly, combining both metals in mixed carbides provides a unique opportunity to couple the metallic functionality of Mo with the oxophilic nature of W, leading to bifunctional catalysts [13, 14]. Previous studies demonstrated that Mo–W interactions can significantly enhance

hydrogenation and HDO performance, lowering carburization temperatures and tuning product selectivity through synergistic effects. The precise Mo:W ratio was also found to strongly influence activity and mechanistic pathways in both thermocatalytic and electrocatalytic reactions [15, 16].

The synthesis process of supported MoW bimetallic carbides directly influences their phase composition, structural properties, and catalytic performance [2]. Controlled synthesis of MoW bimetallic carbides coupled to advanced characterizations at the molecular scale is crucial for understanding the structure-activity relationship. This allows for the adjustment of the optimal composition and phase distribution, enhancing catalytic efficiency, stability, and synergy between Mo and W sites, leading to improved performance in heterogeneous catalysis. The synthesis of TMCs typically relies on temperature-programmed carburization (TPC) or reduction methods, where parameters such as precursor composition, reactive gas, and heating profile dictate the resulting phase [17, 18]. A well-established difference between Mo and W carbides is their distinct carburization behavior: Mo carbides form at significantly lower temperatures than W carbides [19–21]. The addition of Mo has been shown to facilitate the carburization of W, highlighting the importance of cooperative effects during synthesis [15, 20, 21].

However, the role of the order of the carburization sequence in shaping the structure and composition of supported Mo–W carbides has not been systematically investigated. While the influence of the impregnation sequence of the metal precursor has been reported in related bimetallic systems, the impact of stepwise carburization on carbide formation remains poorly explored. Addressing this knowledge gap is crucial for understanding the structure-activity relationship and for rational catalyst design.

In this work, we report on carbon-supported Mo–W carbides prepared by co-impregnation and successive carburization strategies. A combination of x-ray diffraction (XRD), transmission electron microscopy (TEM), and in situ x-ray absorption spectroscopy (XAS) coupled with multivariate curve resolution-alternating least squares (MCR-ALS) analysis is employed to elucidate the influence of preparation route on phase evolution and metal speciation during carburization.

2 | Experimental Part

2.1 | Synthesis

Carbon-supported mono- and bimetallic Mo/W carbides were synthesized by incipient wetness impregnation followed by temperature-programmed carburization (TPC) and passivation. Ammonium heptamolybdate (AHM, Sigma Aldrich, >99%) and ammonium metatungstate (AMT, Sigma Aldrich, ≥85% WO_3 basis) were used as Mo and W precursors, respectively, while NORIT SX1 activated carbon (S_{BET} = 1024 $m^2\ g^{-1}$, pore volume = 1.36 $mL\ g^{-1}$) was used as support. Bimetallic carbides with a Mo:W molar ratio of 3:1 and a total metal surface loading of 0.6 at nm^{-2} (1 mmol of metal per gram of catalyst) were prepared using two different approaches: co-impregnation-carburization and 2-step impregnation-carburization. Weight loadings are summarized in Table S1. In the co-impregnation-carburization method, aqueous solutions of AHM and AMT with the desired molar ratio were mixed, and the resulting solution was impregnated onto the carbon support. In the 2-step sequential impregnation-carburization method, the support was first impregnated with one precursor, carburized and passivated. Then, it was impregnated with the second precursor, followed by a second carburization step and passivation under identical conditions. After impregnation, the samples were dried in air at 100°C for 4 h.

Temperature-programmed carburization (TPC) was performed in a U-shaped quartz reactor using 2 g of precursor material under 20% CH_4/H_2 (total flow = 10 L h^{-1} g^{-1}). The temperature was increased to 600°C at a heating rate of 50°C h^{-1}, maintained for 2 h, and then cooled down to ca. 400°C before quenching to room temperature in a water bath.

To prevent pyrophoric behavior, the resulting samples were passivated under 1% O_2/He (30 L h^{-1} g^{-1}) for 2 h before exposure to air [22]. The final materials were stored in glass vials until use.

For clarity, the samples are denoted as follows. The monometallic samples are referred to as Mo-only and W-only. The bimetallic samples with a nominal Mo:W molar ratio of 3:1 on carbon (Mo_3W_1–C) are denoted according to the preparation route: co-imp. for co-impregnation, W-first when the 2-step sequential impregnation started with AMT, and Mo-first when the 2-step sequential impregnation started with AHM. The sequences of TPC experiments for each sample are schematically summarized in Figure 1.

2.2 | Characterization

The specific surface area and total pore volume of the samples were determined by nitrogen physisorption using a BEL156 analyser. The Brunauer–Emmett–Teller (BET) method was applied to calculate the specific surface area. Prior to the analysis, the samples were degassed under high vacuum (10^{-4} mbar) at 150°C for 4 h. The total pore volume was estimated from the amount of nitrogen adsorbed at relative pressures close to unity. The characteristic pore sizes were derived from Barrett–Joyner–Halenda (BJH) pore size distributions.

The Mo and W contents were quantified by inductively coupled plasma optical emission spectroscopy ICP-OES (Agilent 5100). For the analysis, the samples were mineralized in a 1:1 (v/v) mixture of HNO_3 and HF in Savillex tubes and heated at 100°C for 72 h. After mineralization, the residual carbon support was removed by filtration. The measured values are in good agreement with the nominal loadings, confirming that the synthesis procedures yield the intended Mo:W ratio (Table S1).

Powder x-ray diffraction (XRD) was carried out on a Bruker D8 Advance diffractometer equipped with a Cu Kα radiation source (λ = 1.54184 Å). Diffractograms were recorded over a 2θ range of 10°–90° with a step size of 0.02°.

High-resolution transmission electron microscopy (HR-TEM) images were obtained using a JEOL JEM 2100 microscope operated at 200 keV and equipped with an Oxford Instruments energy-dispersive x-ray (EDX) detector. Additional EDX mapping

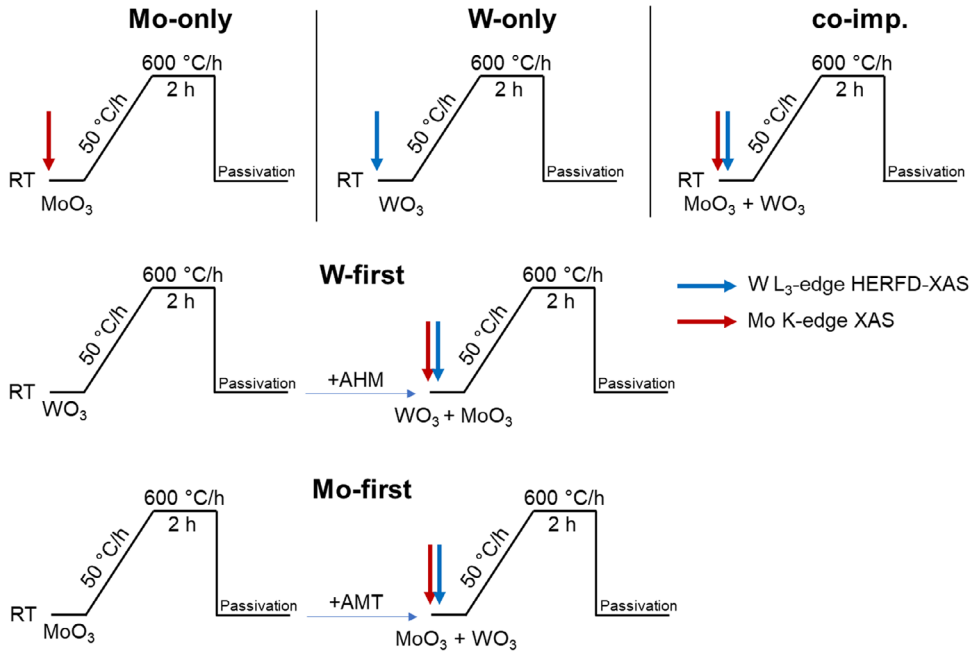

FIGURE 1 | Schematic overview of the Temperature-Programmed Carburization experiments performed for each sample. In addition, arrows indicate the starting point of in situ XAS characterizations: W L_3-edge HERFD-XAS analysis (blue) or Mo K-edge XAS analysis (red). WO_3 and MoO_3 are indicated to clarify the transition metal species involved, but this notation provides no information on the actual speciation of Mo and W. Moreover, in situ XAS experiments do not include the last passivation step.

was performed on a JEOL 2100F field emission electron microscope with a probe size of 0.5 nm to determine the Mo:W atomic ratio. For TEM sample preparation, a small amount of catalyst was suspended in ethanol, ground, sonicated for 3 min, and drop-cast onto a carbon-coated Cu grid. Image analysis was performed using the ImageJ software [23].

X-ray absorption spectroscopy, in particular x-ray absorption near-edge structure (XANES), was performed to follow in situ the carburization of carbon-supported mono- and bimetallic Mo/W samples as well as to characterize their final states. High energy resolution fluorescence detected x-ray Absorption Near Edge Structure (HERFD-XANES) spectra at the W L_3-edge and conventional XAS spectra at the Mo K-edge (20 000 eV) were obtained at the European Synchrotron Radiation Facility (Grenoble, France) on the CRG-FAME-UHD beamline (BM16). The synchrotron ring operated in the top mode at 6 GeV electron energy with a nominal current of 200 mA in 7/8+1 mode. The beamline was equipped with cooled Si (220) double-crystal monochromator surrounded by two Rh-coated mirrors for harmonic rejection. The monochromator energy resolution is 0.335 eV [24]. The beam size on the sample was approximately 200 × 120 µm (H×V, FWHM). The monochromator was energy-calibrated by measuring the tungsten L_3 absorption edge using a metallic tungsten foil (10207 eV).

The W L_3-edge HERFD-XANES spectra were recorded with a crystal analyzer spectrometer (CAS) using seven spherically bent Si (551) crystals in a Rowland geometry. The spectra were recorded at the W Lα1 emission line using a Silicon Drift Detector. The total energy resolution of the HERFD-XANES data was estimated to be approximately 1 eV. In situ XAS experiments were performed using a high-temperature dedicated cell developed at the Neel Institute in Grenoble, France [25]. Approximately 100 mg of the powder sample was loaded into a carbon plug-flow reactor and carburized under 20 vol.% CH_4/H_2 (10 L h^{-1} g^{-1}). All samples were heated to 600°C at 60°C h^{-1} with 2 h isothermal plateaus at 300°C and 600°C. XANES spectra (2 min per scan) were continuously collected during heating, while EXAFS scans ranging up to 10700 eV were recorded at the isothermal steps (7 min per scan). After carburization, the samples were quenched under He flow to room temperature and additional EXAFS spectra were acquired.

Complementary conventional Mo K-edge XAS measurements in both transmission and fluorescence modes were carried out under identical carburization conditions. The same monochromator as for the W L_3-edge was used. The monochromator was energy-calibrated by measuring the molybdenum K-edge using a metallic Mo foil (20000 eV). The fluorescence spectra were acquired using a MIRON 16 element Ge solid-state detector positioned at a 90° to the incident beam. XANES spectra were collected with a typical acquisition time of 4 min per scan, while EXAFS spectra were acquired up to 20 750 eV (15 min per scan).

The sequence of TPC experiments and the corresponding W L_3-edge and Mo K-edge measurements for each sample are schematically summarized in Figure 1.

Ex situ reference spectra were collected for Mo and W oxides, carbides, metallic phases, and a bulk hexagonal MoWC synthesized in-house and confirmed by XRD and STEM-EDX. Additional information on reference preparation and acquisition parameters are provided in the Supporting Information.

To perform chemometric analysis, multivariate curve resolution-alternating least squares (MCR-ALS) was applied to normalized

TABLE 1 | Textural properties of the carbon support and carbide samples obtained by Temperature-Programmed carburization (TPC) at 600°C. All values correspond to passivated materials.

Sample		S_{BET}, $m^2\ g^{-1}$	V_{pore}, $cm^3\ g^{-1}$	d_{pore}, nm
Carbon support		1073	0.71	2.6
Mo-only		726	0.49	2.7
W-only		762	0.49	2.6
Mo_3W_1–C	co-imp.	723	0.51	2.9
	W-first	720	0.52	2.9
	Mo-first	742	0.50	2.8

XANES datasets using the Fastosh software package [26]. The spectral matrix D was decomposed into concentration profiles (C) and pure spectral signatures (S) according to the bilinear model $D = C \times S^T + E$, where S^T denotes the transpose of S and E is the residual error matrix. The number of components was estimated by principal component analysis, and constraints of non-negativity were applied during ALS refinement. Pure components were identified by comparison with reference spectra. All spectra were included in the analysis, including those recorded during the 2 h temperature plateaus, so that both continuous heating and isothermal stages contributed to the resolved component profiles.

3 | Results

The specific surface areas and pore volumes of both carbon support and passivated samples are summarized in Table 1. All materials exhibit a typical type IV isotherm with an H3 hysteresis loop, characteristic of mesoporous carbons. Metal loading led to a decrease of the surface area by about 30% compared to the bare support. Importantly, no significant differences were observed among the carbides, including the bimetallic Mo_3W_1–C samples prepared by the three different routes, which all retained surface areas of ca. 720–740 $m^2\ g^{-1}$ and pore volumes of 0.5 $cm^3\ g^{-1}$. This indicates that neither the Mo:W ratio nor the preparation sequence has a noticeable effect on the textural properties of the catalysts. The decrease compared to the parent carbon is greater than the mass addition of carbide alone and can be attributed to the incorporation of non-porous metal/carbide nanoparticles into the support and possible partial pore plugging during carburization.

XRD analysis was performed to gain insight into the evolution of crystallographic phases in the monometallic and bimetallic samples after carburization. The bare support subjected to temperature-programmed carburization (TPC) conditions also exhibits diffraction features, with signals at 2θ of 26° corresponding to the (002) reflection of the graphitic hexagonal phase (PDF 01-071-3739), as well as additional reflections arising from silica impurities (Figure S1) indicated with stars on Figure 2.

The x-ray diffraction patterns of the mono-metal Mo and W samples, together with the bimetallic Mo_3W_1–C sample prepared by co-impregnation, are shown in Figure 2a. First, it has to be noted that no peaks corresponding to the metal oxide phase were observed by XRD. Thus, the bulk crystal structure of the carbide materials was not affected by the passivation step performed to prevent vigorous oxidation upon exposure to air.

Second, it should be emphasized that due to the similarity of diffraction patterns of Mo and W carbides, as well as Mo–W mixed carbides, the attribution of peaks to a specific phase cannot be entirely unequivocal. Moreover, there is inconsistency in the terminology used for Mo and W carbides. For example, the most thermodynamically stable phase of molybdenum carbide, hexagonal Mo_2C, is referred to in the literature either as α-Mo_2C [27] or β-Mo_2C [28], while the metastable face-centered cubic (fcc) MoC_{1-x} is sometimes described as α-MoC_{1-x} [29] and in other cases as δ-MoC_{1-x} [30]. A similar confusion exists for tungsten carbides, which is further complicated by the multiplicity of polymorphs stable at different temperatures [31]. In this work, we adopt the following notations: α-MoC_{1-x} for the fcc phase and β-Mo_2C for the hexagonal phase, while for W carbides WC_{1-x} and W_2C are used for the cubic and hexagonal phases, respectively.

The monometallic W sample (W-only) exhibits reflections at 2θ = 40°, 58°, 73°, and 86°, corresponding to cubic metallic W (PDF 04-001-2998). Under the standard carburization protocol (600°C, 2 h), the dominant phase is therefore metallic tungsten, in line with literature reports indicating that W is more difficult to carburize than Mo under comparable conditions [20, 32, 33]. However, weak additional shoulders around 36° and 61°–62° relative to the bare support suggests the incipient formation of cubic tungsten carbide. Additional experiments in which the dwell time at 600°C was varied (0, 2, 10 h; Figure S2) indicate that W carburization is kinetically hindered. In contrast, the diffraction pattern of the Mo-only sample contains no metallic reflections. Although the characteristic peaks are broad and significantly overlap with those of the support, the increase in intensity around 2θ of 62° can be assigned to the cubic α-MoC_{1-x} phase (PDF 04-002-0152). The broad diffraction features of the supported samples are consistent with nanosized domains [34], as further confirmed by TEM analysis (Figures 3 and 4). Therefore, TPC of Mo leads to the metastable fcc α-MoC_{1-x} rather than to the more stable hexagonal β-Mo_2C. This can be explained by the effect of the support, which stabilizes the metastable phase due to the very small particle size of the highly dispersed carbide domains [17, 35]. This effect was observed in literature [18, 36]. For example, Shrestha et al. [36] used DFT and thermodynamic analyses to establish particle-size-dependent phase diagrams for Mo and W carbides, showing that fcc phases are stabilized at small sizes, while hexagonal and orthorhombic polymorphs become favored as the crystallites grow larger. For comparison, bulk carburization of AHM salt under identical conditions results in the hexagonal β-Mo_2C phase (Figure S3).

Regarding the bimetallic samples, the diffraction pattern of the co-imp. sample reveals reflections at 2θ of 36°, 42°, and 62°, characteristic of cubic carbides. Importantly, no metallic tungsten peaks are observed, in clear contrast with the monometallic W sample. This indicates that the presence of Mo promotes the carburization of W under the applied conditions. Nevertheless, XRD alone cannot determine whether the reflections arise from a mixture of α-MoC_{1-x} and WC_{1-x} or from a genuine Mo–W bicarbide phase of variable stoichiometry.

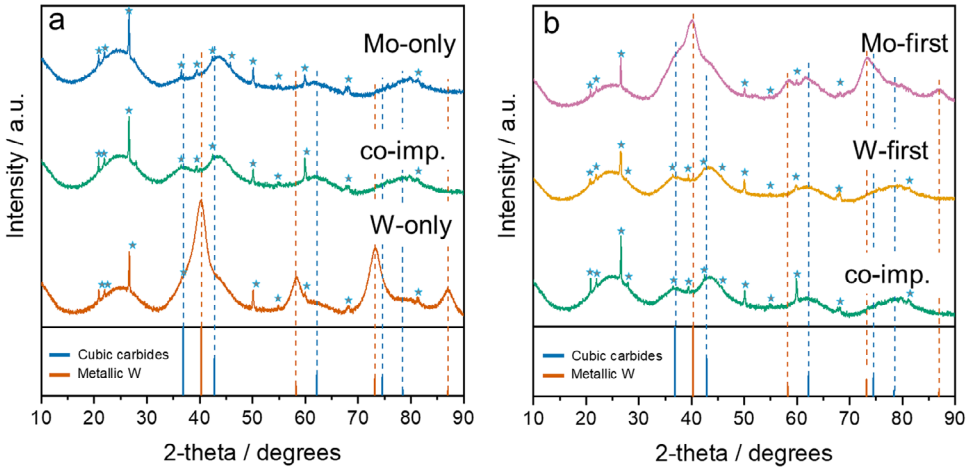

FIGURE 2 | Powder XRD patterns of the passivated samples after Temperature-Programmed Carburization (TPC) up to 600°C. (a) Monometallic Mo-only, W-only, and bimetallic Mo_3W_1–C (co-imp.) compared with reference reflections of cubic carbide phases (e.g., α-MoC_{1-x} phase—PDF 04-002-0152) and bcc metallic W (PDF 04-001-2998). (b) Bimetallic Mo_3W_1–C samples prepared by co-impregnation, W-first, and Mo-first methods. Stars indicate the XRD peaks of the graphitic hexagonal phase and SiO_2 impurities in the bare support.

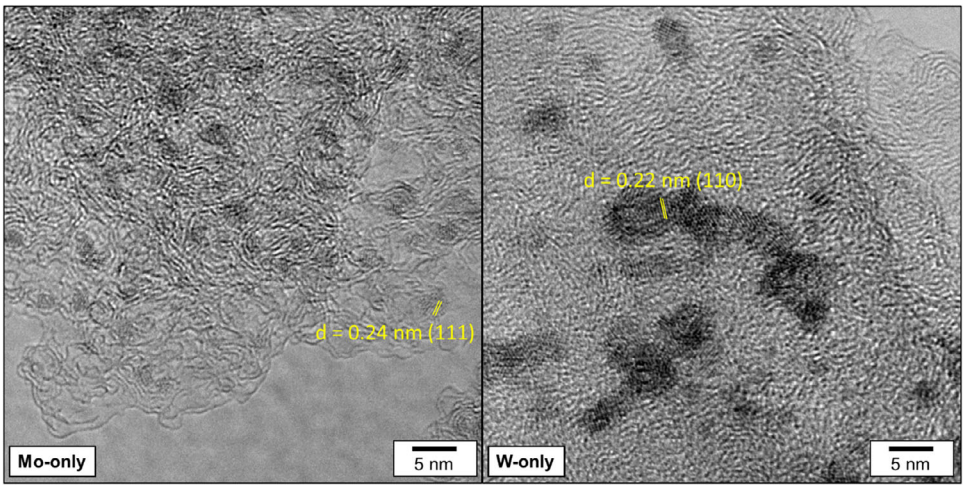

FIGURE 3 | High-resolution TEM images of the mono-metallic samples after Temperature-Programmed Carburization up to 600°C.

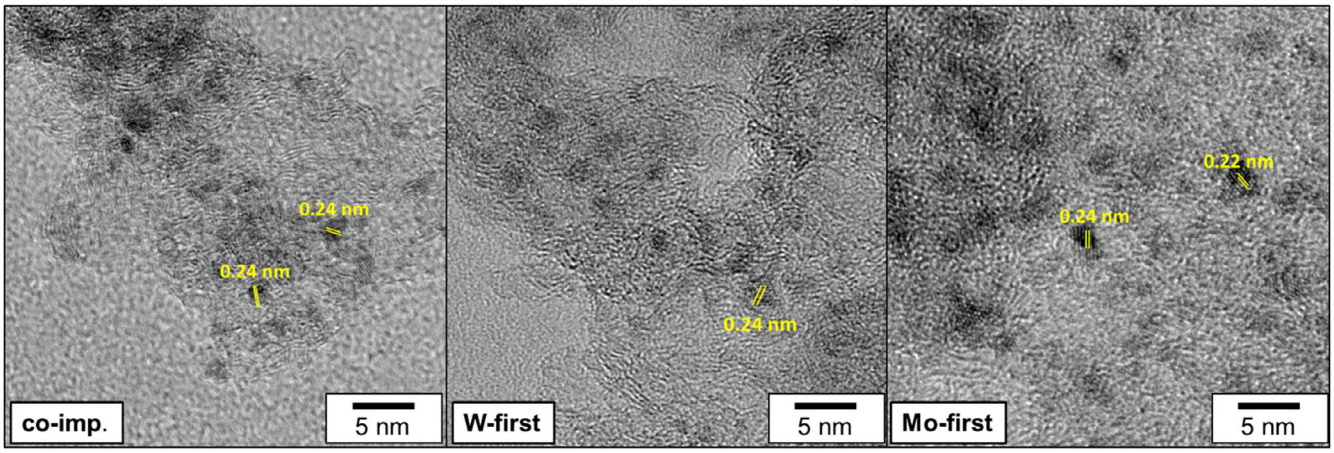

FIGURE 4 | High-resolution TEM images of the bimetallic Mo_3W_1–C samples prepared by co-impregnation, W-first and Mo-first procedures after temperature-programmed carburization (TPC) up to 600°C.

The influence of the preparation method on the composition of Mo_3W_1–C samples after carburization is shown in Figure 2b. It has to be noted that repeated experiments have confirmed the observed XRD patterns (Figure S4). Similar to the co-impregnation method, the W-first sample exhibits only broad reflections of cubic carbide phases, with no metallic W detected. Control experiments, where the second impregnation step of the W-first route was performed using pure water instead of AHM solution, yielded very weak features of metallic W (Figure S5), thereby excluding two-step exposure to water as the sole origin of the absence of metallic W in W-first Mo_3W_1–C sample. Remarkably, when the carburization begins with Mo (Mo-first sample), the diffraction pattern contains both the cubic carbide reflections ($2\theta = 36°, 42°, 62°$) and metallic W peaks ($2\theta = 40°, 58°, 73°, 86°$). Based on TEM (see below and Figure S6), the carbide reflections can be attributed to α-MoC_{1-x}, while the additional peaks correspond to metallic tungsten.

These results suggest that Mo facilitates W carburization only when both elements are transformed simultaneously (co-imp. sample). Once Mo is fully carburized (Mo-first), the W carburization does not seem to happen, W being then only reduced to its metallic state. Overall, the data indicate that cooperative Mo–W interaction favors simultaneous carburization and possibly alloying, thereby promoting the transformation of tungsten into carbide [37, 38].

The TEM images of the passivated samples (Figures 3–4) reveal differences in particle size, phase identity, and composition for the different preparation routes. Particle size distribution histograms are available in Figure S7. The Mo-only sample displays uniformly dispersed nanoparticles on the carbon support. High-resolution TEM shows lattice fringes of d = 0.24 nm, corresponding to the (111) plane of fcc α-MoC_{1-x} (PDF 04-002-0152) with an average particle size below 2.0 nm, confirming that nanoscale dispersion stabilizes the metastable cubic carbide.

In contrast, the W-only sample exhibits larger, partially agglomerated particles, although they remain relatively well distributed on the support. The measured lattice spacing of 0.22 nm matches the (110) plane of cubic metallic W (PDF 04-001-2998). The average particle size is about 4.5 nm, in good agreement with the crystallite size of 4.2 nm determined from Scherrer analysis of XRD peaks. It should be noted, however, that Scherrer analysis reflects coherent diffraction domains and may slightly underestimate full particle dimensions.

For the bimetallic Mo_3W_1–C samples, the average particle size lies between those of the monometallic carbides (2.4–3.6 nm depending on preparation). In the co-impregnated material (particle size = 2.6 nm), particles are more homogeneously distributed than in W-only, and HRTEM reveals only carbide lattice spacings. STEM-EDX analysis on numerous single particles demonstrates the simultaneous presence of both Mo and W suggesting the presence of bimetallic single particles. While the overall Mo:W ratio determined by ICP-OES corresponds to the targeted 3:1 composition (Table S1), individual particles show variability (e.g., 40:60, 43:57, 39:61; Table S2). Bimetallic particles seem to be richer in W. Hence, the presence of (small) monometallic Mo carbide particles cannot be excluded.

The sequential carburization route yields more contrasted results. When W is carburized first (W-first), the resulting sample resembles the co-impregnated one: particle sizes remain in the intermediate range (= 2.5 nm), and EDX results (Table S2) confirm a simultaneous presence of Mo and W, consistent with the formation of mixed carbides at the single particle level. By contrast, the Mo-first sample exhibits more pronounced agglomeration. The particle size distribution (Figure S7) suggests two particle populations characterized by distinct mean sizes (3.6 nm and 2.4 nm). Although TEM analysis alone does not allow one an unambiguous assignment of particle size to a specific phase, HRTEM analysis (Figure S6) reveals lattice spacings consistent with both metallic W and α-MoC_{1-x}. Considering these observations together, the bimodal distribution may reflect the coexistence of two material populations, with the larger particles likely related to metallic W domains and the smaller ones to Mo carbide.

Overall, the size trend follows Mo-only (< 2.0 nm) < Mo_3W_1–C (= 2.4–3.6 nm) < W-only (= 4.5 nm). The stabilization of smaller crystallites in the bimetallic samples is likely facilitated by Mo–W alloying and associated strain effects, which hinder coarsening. [15, 21] Conversely, residual metallic W in the Mo-first route is consistent with particle growth and agglomeration.

3.1 | X-ray Absorption Spectroscopy

XANES analysis of the mono- and bimetallic Mo/W samples has been performed during temperature-programmed carburization (TPC). XANES is particularly appropriate for monitoring in situ the evolution of the oxidation state and local coordination of metal centers, thereby complementing diffraction-based techniques that probe only long-range crystalline order. It provides thus valuable insights into the dynamic structural evolution of the catalysts [39–41]. To extract quantitative and kinetically meaningful information from the evolving spectra, we combined conventional XANES descriptors (edge position, white-line intensity, pre-edge features) with chemometric analysis by MCR-ALS. This approach allows one to decompose XANES series into pure components in order to track their temperature-dependent evolution [42–44]. For all datasets (mono- and bimetallic samples), MCR-ALS analysis consistently converged to three pure components for describing the temperature evolution of the metal speciation. This choice was guided by (i) the scree plots obtained from Principal Component Analysis (PCA) (Figures S8 and S9), (ii) the structural analogy with reference compounds, and (iii) the internal consistency of the temperature evolution across datasets. Attempts with four components yielded an additional factor that was essentially redundant, showing similar spectral features and temperature evolution as one of the three selected components. Therefore, the three-component model was retained throughout, ensuring comparability between the mono- and bimetallic systems.

The spectra of well-defined W- and Mo-containing reference compounds, together with their discussion and calibration of spectral features against oxidation state, are presented in the Supporting Information (Figures S10 and S11). It should be noted that the reference spectra used for comparison with the MCR-ALS pure components correspond to bulk crystalline compounds,

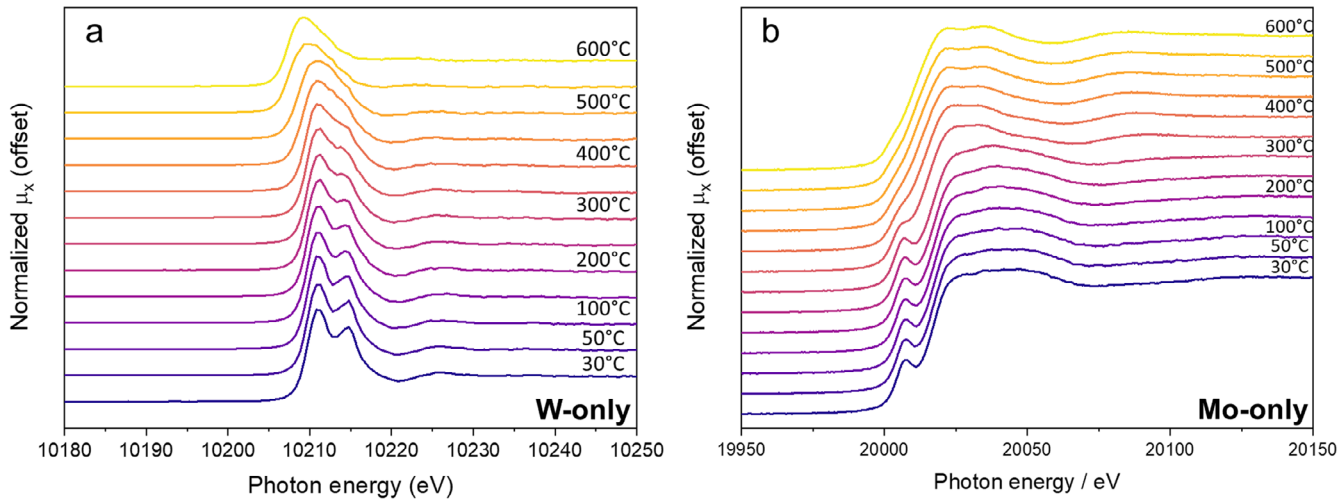

FIGURE 5 | Temperature-resolved of (a) W L_3-edge HERFD-XANES spectra of the W-only and (b) conventional Mo K-edge XANES spectra of the Mo-only samples during temperature-programmed carburization (TPC). Spectra are shown from room temperature to 600°C in 50°C increments.

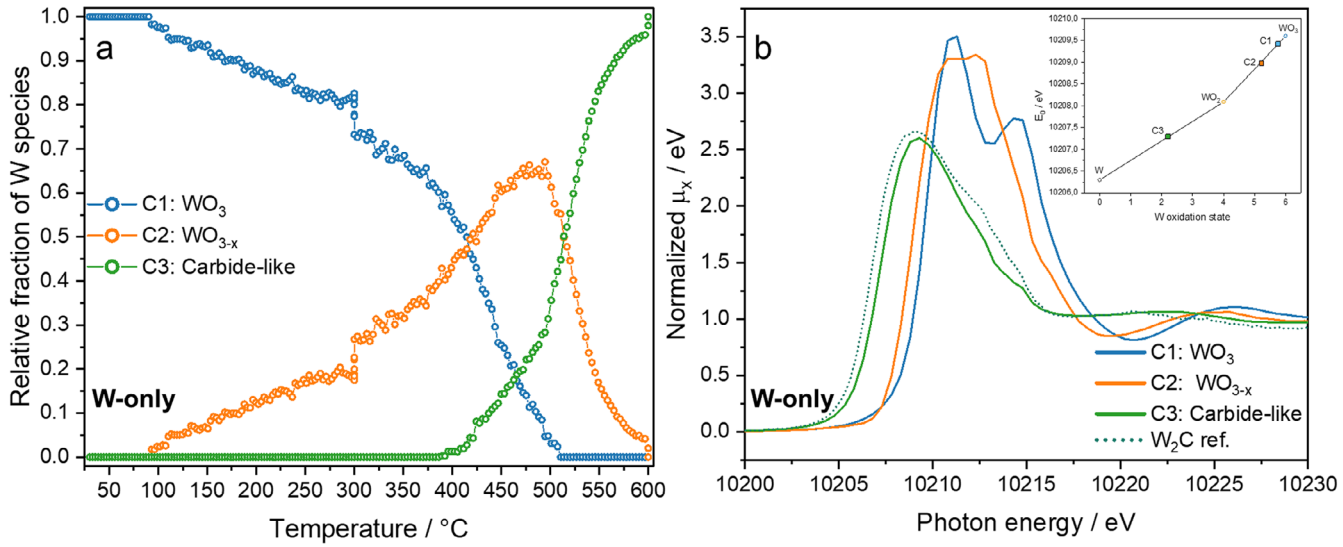

FIGURE 6 | MCR-ALS results for the W L_3-edge during Temperature-Programmed Carburization (TPC) of the monometallic W-only sample. (a) Evolution of concentration profiles of three spectral components as a function of temperature. The higher density of points at 300°C and 600°C reflects the 2 h plateaus applied during the in situ experiment. (b) Corresponding pure component spectra extracted by MCR-ALS. Inset: Position of the edge energy (E_0) of the pure components (C1, C2 and C3) on the calibration curve derived from W reference compounds (Figure S10).

whereas the samples under study consist of highly dispersed species supported on carbon. Such dispersion and metal-support interactions can alter the local coordination and electronic structure, leading to subtle shifts in edge position and white-line intensity relative to the bulk references [45].

3.1.1 | W L_3-edge Analysis

The W L_3-edge HERFD-XANES spectra recorded during TPC for the W-only sample are shown in Figure 5a and the full set of spectra for all samples in Figure S12. The MCR-ALS deconvolution for the W-only sample is presented in Figure 6. At low-moderate temperature (≤ 400°C), spectra are dominated by a first component (C1) with edge energy (E_0 = 10209.4 eV) and an intense, clearly split white line, closely match the AMT/WO_3 references (Figure S10) and indicate W^{6+} in octahedral coordination [46]. The use of HERFD is crucial here, as the enhanced energy resolution allows us to resolve the characteristic doublet structure of the white line for W^{6+}, which would be largely smeared out in conventional XANES and thus provides a sensitive probe of subtle electronic and coordination changes around W.

Between 300°C–500°C, the oxide fraction declines while a reduced WO_{3-x} component (C2) grows, this component exhibits a slight shift of E_0 to lower energy with a decrease and partial collapse of the white-line doublet, consistent with an oxygen-deficient mixed phase positioned between WO_3 and WO_2 references. Above 400°C, the reduced WO_{3-x} fraction is progressively replaced by a third component (C3) whose spectral features (lower overall white-line intensity, broadening and merging of the doublet and a shift of the white line maximum to 10206.9 eV)

are consistent with the W_2C reference and increased W–C covalency/metallic character [47]. Thus, the HERFD-XANES MCR-ALS analysis reveals a three-component sequence during temperature-programmed carburization: oxide → reduced oxide (WO_{3-x}) → carbide-like, with the evolution of the split white line providing a particularly sensitive marker of the gradual transition from W–O to W–C coordination.

Notably, while the final (C3) MCR-ALS component shows the closest similarity to the hexagonal W_2C reference for the W-only sample, ex situ XRD (Figure 2) reveals predominantly metallic W, accompanied by minor reflections corresponding to a cubic, non-stoichiometric carbide phase. The apparent discrepancy between XRD and XAS results may arise from the different length scales probed by the two techniques. While XRD shows that the final solid retains the bcc structure of metallic W, HERFD-XANES data reveal increasingly pronounced W–C bonding and a characteristic modification of the white-line doublet, consistent with early-stage carbon uptake at interstitial sites. Hence, it may be concluded that, up to 600°C for the W-only sample, the local electronic environment around W becomes carbidic (HERFD-XAS), while the material still retains its bcc crystallographic structure (XRD). Such transient, nonstoichiometric WC_x phases, in which local carbidic coordination precedes a full lattice transformation, are well documented during early stages of tungsten carburization [48, 49]. This cubic WC_{1-x} phase, frequently reported for carbon-supported carbides, is not available in bulk crystalline form, which explains its absence from the reference library; the same also concerns the MoC_{1-x} cubic carbide reference.

The MCR-ALS results of the W L_3-edge spectra for the three bimetallic samples are shown in Figures S13–S15 and the full set of spectra in Figure S12. As for the monometallic W system, the main components are obtained and can be assigned to oxide (C1), reduced-oxide (C2), and carbide-like/carbide (C3) species. The characteristic of the C3 component raises also an apparent discrepancy between XRD (Figure 2) and XAS for the Mo-first sample (Figure S15): C3 appears predominantly carbidic and close to W_2C in HERFD-XANES, whereas XRD still shows reflections of metallic W. As postulated for the W-only case this contrast can be rationalized by the different structural sensitivities of the two techniques: HERFD-XANES detects local W–C bonding and the associated modification of the white-line doublet before the long-range lattice rearranges, while XRD continues to probe a predominantly metallic bcc phase until carbon incorporation becomes extensive.

To visualize the evolution of the carbidic environment across all compositions, the C3 spectra of the four W-containing samples are compared in Figure 7. All spectra display the characteristic broad white line with attenuated post-edge features that signify W–C coordination. Yet, two distinct spectral families can be distinguished. For the co-impregnated (green spectra in Figure 7) and W-first (yellow spectra in Figure 7) samples, a systematic shift of the white-line maximum to higher energy (~0.6 eV) is observed, together with a more structured post-edge region, indicative of a less metallic, more strongly carbidic environment. In contrast, the W-only and Mo-first samples show a lower white-line E_0 consistent with a carbide-like but more metallic character consistent with XRD showing reflections of metallic W. These subtle but systematic differences, resolved by HERFD-XANES,

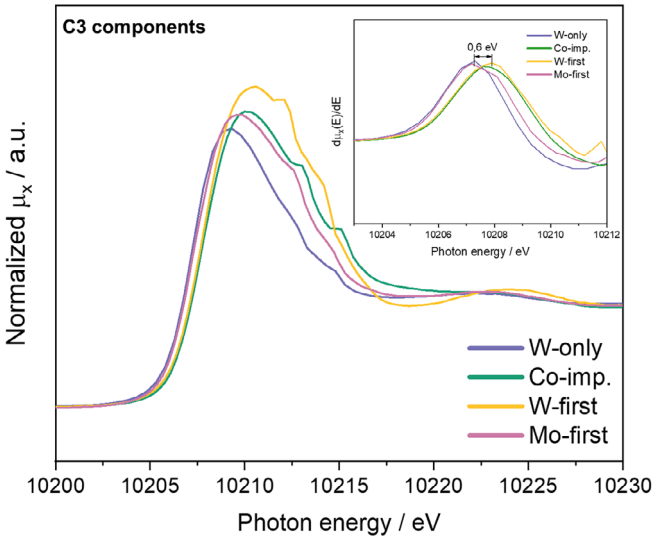

FIGURE 7 | Comparison of the carbide-like (C3) components extracted by MCR-ALS from the W L_3-edge XANES spectra of the four samples studied. The main panel shows the normalized C3 spectra of pure components. The inset presents the first derivatives of the same spectra.

highlight the strong influence of synthesis sequence on the local W environment during carburization and underscore the added value of HERFD for in situ studies of tungsten carbides, which remain scarcely documented in the literature.

These spectral differences confirm XRD results and show that two different local electronic environments are formed depending on the preparation route. For the W-only and Mo-first samples the metallic W (bcc) environment probed with XRD corresponds to non-stoichiometric $W–C_{1-x}$ domains probed with XAS where carbon occupies interstitial sites in a structure that retains its bcc metallic lattice. For the co-imp. and W-first samples a Mo–W carbide environment is detected both with XAS and XRD. Moreover, in the co-imp. and W-first samples, stronger Mo–W mixing may facilitate deeper carbon insertion and structural reorganization, producing a genuine mixed Mo–W carbide that is detected by both methods.

The temperature-resolved evolution of the three MCR-ALS components (oxide → reduced oxide → carbide/carbide-like) for the bimetallic samples at the W L_3-edge is summarized in the predominance-window diagram (Figure 8). One may refer to Figure 1 to follow the preparation route and the step at which XANES analysis is performed.

In the co-impregnated sample, the oxide fraction remains dominant up to 250°C only, a temperature significantly lower that for W only (420°C). Similarly, for co-imp. the carbide-like fraction grows gradually, reaching 10% at 366°C (vs. 424°C for W-only) and becoming dominant 50°C earlier than for W-only. The lower temperatures of transition of the "oxide → reduced oxide → carbide-like" sequence for the co-imp. sample with respect to W-only suggest the existence of mixed MoO_2-WO_{3-x} domains, consistent with the intimate oxide mixing promoted by co-impregnation in the co-imp. sample promoting the reduction/carburization of tungsten by molybdenum.

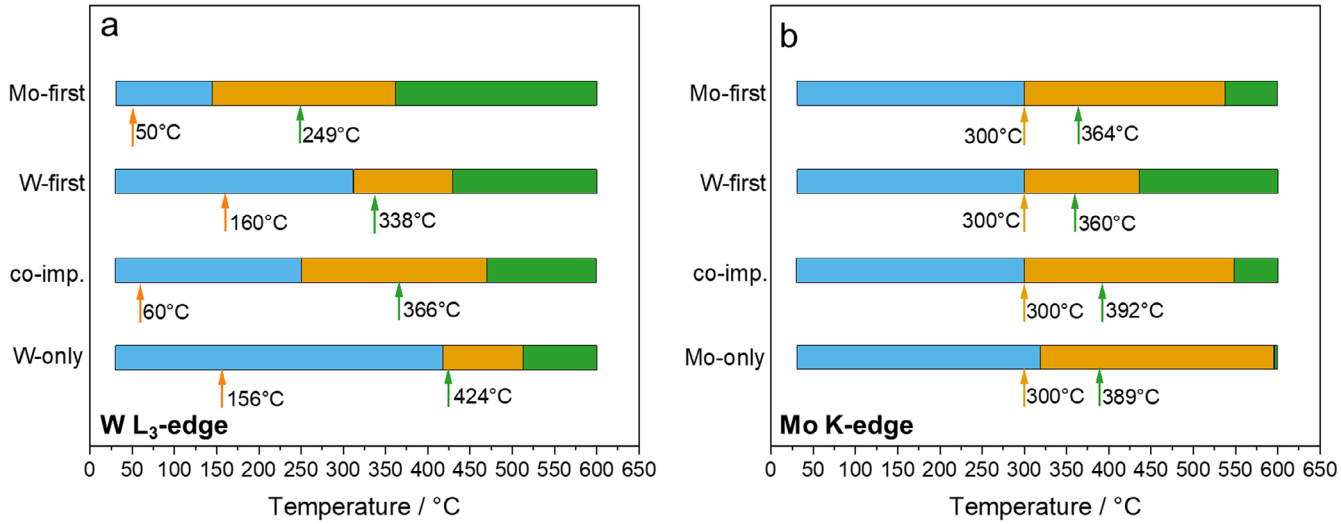

FIGURE 8 | Temperature "predominance windows" of oxide (blue), reduced oxide (orange), and carbide/carbide-like (green) components extracted by MCR-ALS from in situ XANES during Temperature-Programmed Carburization (TPC). (a) W L_3-edge and (b) Mo K-edge analyses. Orange and green arrows indicate the onset temperatures (T_{onset}) for the appearance of the C2 (reduced-oxide) and C3 (carbide-like) components, respectively, defined as the temperature at which the corresponding species reaches 10% of its maximum fractional contribution.

In the W-first sample, it should be noted that XANES analysis starts after Mo impregnation following the first W impregnation-carburization-passivation sequence (Figure 1). Figure S14 shows that W was fully reoxidized during the subsequent Mo impregnation step, as component C1 is entirely oxidic. The temperature evolution of the W-first sample (Figure 8a) closely resembles that of the co-impregnated sample, indicating that intimate oxide mixing also occurs after Mo impregnation. Hence, both routes lead to similar outcomes, as already evidenced by XRD (Figure 2b). The main noticeable difference arises from the higher stability of the W oxide component, which persists to higher temperatures (310°C for W-first vs. 250°C for co-imp.). This delay likely results from the kinetic constraint imposed by the passivated W phase in W-first, which becomes activated only after Mo reduction progresses.

For the Mo-first sample, all transitions are shifted to much lower temperatures. This sample shows the earliest loss of oxide dominance (145°C) and the lowest temperature for the rise of the carbide component, which appears at 249°C and becomes dominant above 360°C. The pre-existence of reduced Mo domains (as discussed below) formed during the first Mo impregnation-carburization-passivation sequence (Figure 1) likely promotes W reduction and carburization, thereby suppressing the induction period observed in the W-first route.

3.1.2 | Mo K-edge Analysis

The Mo K-edge XAS spectra recorded during TPC for the Mo-only sample is shown in Figure 5b and the full set of spectra for all samples is given in Figure S16. The corresponding MCR-ALS analysis is presented in Figures 9 and S17–S19. Chemometric analysis of the Mo-only sample (Figure 9) resolves three main components: oxide (C1), reduced-oxide (C2), and carbide (C3) revealing the same oxide → reduced oxide → carbide sequence as for the W L_3-edge. However, two differences may be highlighted with respect to the W case. First, the C2 (reduced-oxide) component appears more reduced at an edge position consistent with MoO_2 (see the inset in Figure 9b). Second, the edge position of the C3 component lies at a slightly higher energy than that of the carbide references (Mo_2C and MoWC, Figure S11), while XRD demonstrates the presence of carbide nanoparticles after TPC (Figure 2). This shift may be explained by two factors: (i) the nanometric size of the supported molybdenum carbide particles that may lead to a strong metal-support interaction and (ii) the presence of tungsten for bimetallic samples. Both effects likely decrease the electron density around the Mo center and thus shift E_0 to higher energy.

The temperature evolution of all pure components obtained from MCR-ALS is summarized in the predominance-window diagram (Figure 8b). It can be noted that part of the reduction-carburization sequence occurs during the 2 h temperature plateaus at 300 and 600°C (see abrupt changes in Figures 9 and S15–S19) which imply that reduction and carburization of Mo may be under kinetic control [50–52]. In contrast to the W case, Figure 8b shows that the stability domain of the oxidic C1 component, as well as the onset of C2 (MoO_2) formation, are only weakly affected by the preparation route, since most of the changes occur during the 2 h plateau at 300°C. For all samples, the oxide component remains dominant up to 300°C, where the first reduction step of Mo(VI) to MoO_2 under CH_4/H_2 occurs. The C2 component then becomes predominant, preceding carburization.

The onset of Mo carbide formation (C3 component, green arrow) is also very similar among the samples (within a 30°C range), indicating that the initiation of Mo carbide formation is only weakly dependent on the preparation route. All samples are fully carburized after the 600°C plateau. Nonetheless, the predominance of Mo carbides (green area, Figure 8b) starts at a lower temperature for the bimetallic Mo–W carbides than for the Mo-only sample, implying that the presence of W facilitates Mo carburization.

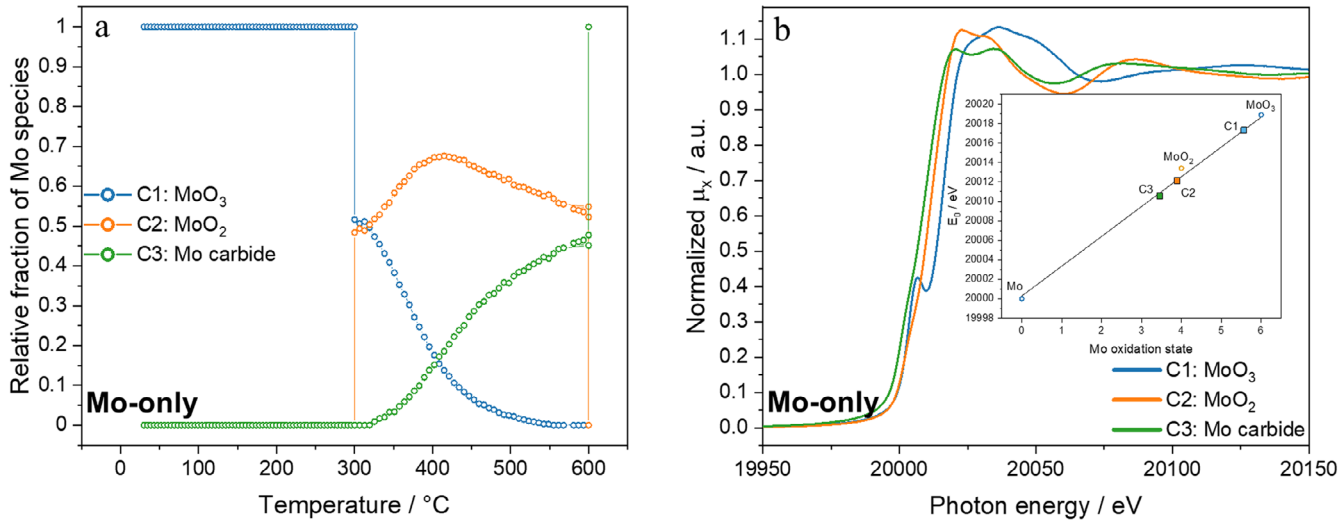

FIGURE 9 | MCR-ALS results of the Mo K-edge XANES during Temperature-Programmed Carburization (TPC) of Mo-only sample. (a) Temperature evolution of the resolved spectral components. The vertical lines correspond to the 2 h plateaus applied during the in situ experiment at 300°C and 600°C. (b) Corresponding pure component spectra, with their edge energies positioned in the E_0-oxidation state calibration plot (inset, Figure S11).

4 | Discussion

Figure 10 schematically illustrates the sequential transformations occurring during carburization and their dependence on the synthesis route. It highlights the progressive evolution from oxides to reduced oxides and finally to carbides, together with the characteristic onset temperatures deduced from MCR-ALS analysis (Figure 8). The scheme emphasizes that the relative temperature and overlap of the MoO_2 and WO_{3-x} transformation domains (Figure 8) determine whether the carburization proceeds through cooperative oxide-oxide interactions or through separate, route-dependent pathways.

For the monometallic references, the W-only sample undergoes a slow and gradual reduction toward a sub-oxide WO_{3-x} starting near 150°C, with the late carburization step occurring only above 420°C. This delayed conversion reflects the high stability of WO_{3-x} species under carburizing conditions [46]. In contrast, Mo-only begins to reduce more extensively to MoO_2 at higher temperature (300°C) but starts to convert into Mo carbide at a slightly lower temperature of 390°C. These monometallic samples serve as benchmarks for evaluating the behavior of the bimetallic systems.

In the co-impregnated sample, both metals evolve in parallel, with broad coexistence of MoO_2 and WO_{3-x} intermediates extending up to 480°C. This overlap of reduced oxide domains promotes intimate oxide-oxide interactions and the progressive formation of mixed Mo–W carbide species, which finally transform into Mo–W carbide domains (MoWC). Carburization starts at around 380°C for both metals, significantly earlier than in the W-only reference showing the promotion effect of Mo. The schematic in Figure 10 depicts this route as a nearly synchronous reduction and carburization sequence, driven by the simultaneous availability of both oxides in contact.

The W-first sample follows almost the same cooperative principle but slightly shifted in temperature. The initially passivated WO_x species persist to higher temperature, and W reduction proceeds more abruptly once initiated. Nevertheless, both metals undergo reduction within a similar temperature domain, and their reduced-oxide intermediates coexist mainly at high temperature, up to around 420°C. The persistence of MoO_2 and WO_{3-x} species in this upper range promotes oxide-oxide interactions before the onset of carburization leading to mixed Mo–W carbide domains. This behavior reflects a cooperative oxide-oxide pathway comparable to that of the co-impregnated sample.

The Mo-first route follows a different carburization mechanism respect to co-imp. and W-first with a very low onset of W reduction since WO_{3-x} becomes predominant at about 150°C (orange area, Figure 8). This may be explained by the existence of reduced Mo domains before W introduction that are able to activate hydrogen. In fact, after the first carburization step, MoC_{1-x} domains are formed but are partially re-oxidized during passivation (component C1 at the Mo-edge in Figure S19). However, this oxidic component appear with a E_0 (20016.2 eV, Figure S19) 1 eV lower than that of the C1 component of the co-imp. and W-first samples (20017.7 and 20017.3 eV, respectively, Figures S17–S18) where the starting Mo compound is undoubtedly Mo^{6+} (AHM). Hence, for the Mo-first sample, the molybdenum speciation at the beginning of the second W impregnation-carburization sequence is presumably a sub-stoichiometric MoO_{3-x} phase that can promote tungsten reduction and the following carburization as early as 250°C, far below the temperatures observed for other routes (around 350°C for co-imp. and W-first, 420°C for W-only). The predominance window in Figure 8 illustrates how this premature W reduction shortens the MoO_2–WO_{3-x} coexistence window to a narrow domain around 300°C–360°C. Because of this limited overlap, the two metals follow largely independent transformation paths, leading to the formation of separate Mo-rich and W-rich carbide phases rather than a homogeneous bimetallic compound.

Overall, the comparison of the pathways presented in Figure 10 demonstrates that the preparation sequence controls the width

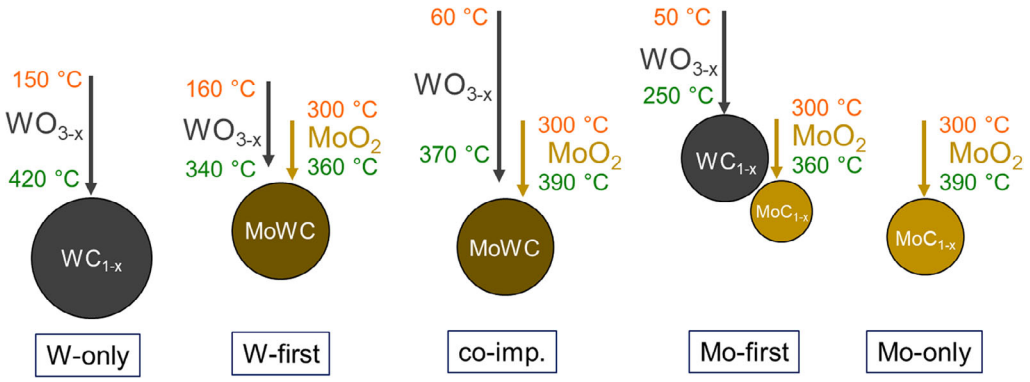

FIGURE 10 | Schematic illustration of the sequential transformations during carburization of Mo–W precursors for the different preparation routes. The scheme displays only the transformation steps that were monitored by in situ XAS during the temperature-programmed carburization corresponding to the transition from the orange region (partially reduced phases) to the green one (carbidic phases) in Figure 8. Temperatures refer to appearance of the reduced oxide (orange) or the carbide (green), as indicated by arrows in Figure 8 (temperatures are rounded to the nearest ten). The circles are schematically proportional to the size of the nanoparticles as determined from TEM. The arrows and their positions are schematically proportional to the temperature span between the appearance of the reduced oxide and the appearance of the carbide.

and temperature of the MoO_2–WO_{3-x} coexistence window, which in turn dictates the nature of the carburization mechanism. Co-impregnation and W-first routes feature extended overlapping domains that favor cooperative oxide-oxide transformations and yield mixed Mo–W carbides. In contrast, the Mo-first route exhibits an early W reduction, hence a narrow MoO_2–WO_{3-x} coexistence domain leading to segregated products. The systematic shift of the W-carbide onset temperature (green arrows in Figure 8a) from 424°C in the W-only sample to 249°C in the Mo-first one visualizes this progressive facilitation of W carburization in the presence of Mo species.

5 | Conclusions

This work establishes a direct relationship between the preparation routes of carbon-supported Mo–W bimetallic carbides and the sequence of reduction and carburization events to explain the speciation of the supported nanophases upon temperature-programmed carburization (TPC) at 600°C in CH_4/H_2. XRD and TEM show that for Mo and W co-impregnation or sequential impregnation-carburization of W-first, bimetallic carbides are formed at the single particle level after TPC. Conversely, sequential impregnation of Mo-first lead to segregated particles of 2.5–3.5 nm: Mo-rich and W-rich carbide-like nanophases. Combination of XRD and XAS results show that the W-rich nanoparticles in the latter case are most probably transient, nonstoichiometric WC_x phases retaining the metallic bcc structure (XRD) with a local carbide environment (XAS). By combining in situ HERFD-XAS at the W edge, conventional in situ XAS at the Mo edge and chemometric MCR-ALS analysis, the predominance domains of oxide, reduced oxide, and carbide components formed upon temperature-programmed carburization are disentangled with unprecedented details.

A clear order of carburization is identified, governed not only by the intrinsic reducibility of the metals but also by the extent of overlap between the predominance domains of reduced MoO_2 and WO_{3-x} as well as by the presence of pre-carburized Mo domains. When Mo and W are carburized simultaneously (co-impregnation) or when sequential impregnation is performed with W first, the large coexistence of reduced MoO_2 and WO_{3-x} domains enable cooperative oxide-oxide transformations and favor mixed bimetallic carbide formation. When the sequential impregnation-carburization is performed with Mo-first, XAS shows that W deposition occurs next to a preformed reduced MoO_{3-x} matrix that may accelerate W carburization through hydrogen activation. Enhanced W reduction/carburization limits interdiffusion with Mo nanoparticles yielding segregated Mo-rich and W-rich carbides.

These findings have direct implications for catalysis. Transition metal carbides are valued as noble-metal alternatives, combining metallic and oxophilic functionalities. Our results show that the synthetic pathway dictates whether such functionalities coexist within intimately mixed domains or remain in spatially segregated particles. The degree of Mo–W mixing achieved during carburization will likely control activity and selectivity.

In the present work, the combination of advanced in situ spectroscopy and chemometric analysis has revealed that the sequence of precursor impregnation and carburization are decisive parameters for tailoring Mo–W carbides. It becomes possible to steer the material either toward homogeneous bimetallic supported nanoparticles or toward phase-separated carbides thus laying the foundation for rational catalyst design.

Acknowledgments

The authors gratefully acknowledge Ferdaous Ben Romdhane (TEM), Saremblé Koné-Guira (Surface area measurements, ICP-OES), Laetitia Valentin (ICP-OES), and Mohamed Selmane (XRD) for their valuable assistance with characterization. The TEM platform of FCMat is acknowledged for access to analytical facilities. X-ray absorption experiments were performed at the BM16 (FAME-UHD) beamline of the ESRF (Grenoble), and the authors thank the beamline staff for their technical support during the measurements. This work was supported by the French National Research Agency (ANR) under the project HYDROCARB (ANR-22-CE07-0043).

Open access publication funding provided by COUPERIN CY26.

Conflicts of Interest

The authors declare no conflict of interest

Data Availability Statement

The data that support the findings of this study are available in the supplementary material of this article.

References

1. R. B. Levy and M. Boudart, "Platinum-Like Behavior of Tungsten Carbide in Surface Catalysis," *Science* 181 (1973): 547–549, https://doi.org/10.1126/science.181.4099.547.

2. S. T. Oyama, "Preparation and Catalytic Properties of Transition Metal Carbides and Nitrides," *Catalysis Today* 15 (1992): 179–200, https://doi.org/10.1016/0920-5861(92)80175-M.

3. G. S. Ranhotra, A. T. Bell, and J. A. Reimer, "Catalysis Over Molybdenum Carbides and Nitrides: II. Studies of CO Hydrogenation and C_2H_6 Hydrogenolysis" *Journal of Catalysis* 1987, 108, 40–49.

4. M.-L. Frauwallner, F. López-Linares, J. Lara-Romero, et al., "Toluene Hydrogenation at Low Temperature Using a Molybdenum Carbide Catalyst," *Applied Catalysis A: General* 394 (2011): 62–70, https://doi.org/10.1016/j.apcata.2010.12.024.

5. B. Dhandapani, T. St Clair, and S. T. Oyama, "Simultaneous Hydrodesulfurization, Hydrodeoxygenation, and Hydrogenation With Molybdenum Carbide," *Applied Catalysis A: General* 168 (1998): 219–228, https://doi.org/10.1016/S0926-860X(97)00342-6.

6. F. H. Ribeiro, R. A. Dalla Betta, M. Boudart, J. Baumgartner, and E. Iglesia, "Reactions of Neopentane, Methylcyclohexane, and 3,3-dimethylpentane on Tungsten Carbides: The Effect of Surface Oxygen on Reaction Pathways," *Journal of Catalysis* 130 (1991): 86–105, https://doi.org/10.1016/0021-9517(91)90094-K.

7. E. Iglesia, F. H. Ribeiro, M. Boudart, and J. E. Baumgartner, "Synthesis, Characterization, and Catalytic Properties of Clean and Oxygen-modified Tungsten Carbides," *Catalysis Today* 15 (1992): 307–337, https://doi.org/10.1016/0920-5861(92)80181-L.

8. X. Du, R. Zhang, D. Li, C. Hu, and H. Garcia, "Molybdenum Carbide as Catalyst in Biomass Derivatives Conversion," *Journal of Energy Chemistry* 73 (2022): 68–87, https://doi.org/10.1016/j.jechem.2022.05.014.

9. K. Wu, C. Yang, Y. Zhu, et al., "Synthesis-Controlled α- and β-Molybdenum Carbide for Base-Promoted Transfer Hydrogenation of Lignin to Aromatic Monomers in Ethanol," *Industrial & Engineering Chemistry Research* 58 (2019): 20270–20281, https://doi.org/10.1021/acs.iecr.9b04910.

10. M. Führer, T. van Haasterecht, and J. H. Bitter, "Molybdenum and Tungsten Carbides Can Shine Too," *Catalysis Science & Technology* 10 (2020): 6089–6097.

11. L. Leclercq, M. Provost, H. Pastor, and G. Leclercq, "Catalytic properties of transition metal carbides II. Activity of bulk mixed carbides of molybdenum and tungsten in hydrocarbon conversion," *Journal of Catalysis* 117 (1989): 384–395, https://doi.org/10.1016/0021-9517(89)90349-7.

12. T. Shao, L. Li, and J. Lin, "Noble-metal-Like catalysts of carbide and nitride for the low-temperature water–gas shift reaction: A review," *Catalysis Science & Technology* 15 (2025): 1339–1356, https://doi.org/10.1039/D4CY01298D.

13. C.-C. Cheng, T.-Y. Lin, Y.-C. Ting, S.-H. Lin, Y. Choi, and S.-Y. Lu, "Metal-organic Frameworks Stabilized Mo and W Binary Single-atom Catalysts as High Performance Bifunctional Electrocatalysts for Water Electrolysis," *Nano Energy* 112 (2023): 108450, https://doi.org/10.1016/j.nanoen.2023.108450.

14. A. M. Robinson, J. E. Hensley, and J. W. Medlin, "Bifunctional Catalysts for Upgrading of Biomass-Derived Oxygenates: A Review," *ACS Catalysis* 6 (2016): 5026–5043, https://doi.org/10.1021/acscatal.6b00923.

15. C.-C. Tran, Y. Han, M. Garcia-Perez, and S. Kaliaguine, "Synergistic effect of Mo–W carbides on selective hydrodeoxygenation of guaiacol to oxygen-free aromatic hydrocarbons," *Catalysis Science & Technology* 9 (2019): 1387–1397, https://doi.org/10.1039/C8CY02184H.

16. A. Mehdad, R. E. Jentoft, and F. C. Jentoft, "Single-phase Mixed Molybdenum-tungsten Carbides: Synthesis, Characterization and Catalytic Activity for Toluene Conversion," *Catalysis Today* 323 (2019): 112–122, https://doi.org/10.1016/j.cattod.2018.06.037.

17. A. D. Zanet and S. A. Kondrat, "A Review of Preparation Strategies for α-MoC1–x Catalysts," *Johnson Matthey Technology Review* 66 (2022): 285–315, https://doi.org/10.1595/205651322X16383716226126.

18. P. Schlachta, R. E. Jentoft, F. C. Jentoft, and K. Köhler, "Synthesis of Phase-Pure W_2C and WC by Separation of Reduction and Carburization and Their Differing Performance as Hydrogenation Catalysts," *The Journal of Physical Chemistry C* 129 (2025): 20907–20921, https://doi.org/10.1021/acs.jpcc.5c05153.

19. L. C. A. Bastos, W. R. Monteiro, M. A. Zacharias, G. M. da Cruz, and J. A. J. Rodrigues, "Preparation and Characterization of Mo/W Bimetallic Carbides by Using Different Synthesis Methods," *Catalysis Letters* 120 (2008): 48–55, https://doi.org/10.1007/s10562-007-9248-9.

20. M. Führer, T. van Haasterecht, E. J. J. de Boed, P. E. de Jongh, and J. H. Bitter, "Synthesis and Characterization of Supported Mixed MoW Carbide Catalysts," *The Journal of Physical Chemistry C* 127 (2023): 7792–7807.

21. Q. Fu, B. Peng, J. Masa, et al., "Synergistic Effect of Molybdenum and Tungsten in Highly Mixed Carbide Nanoparticles as Effective Catalysts in the Hydrogen Evolution Reaction Under Alkaline and Acidic Conditions," *ChemElectroChem* 7 (2020): 983–988, https://doi.org/10.1002/celc.202000047.

22. A. Mehdad, R. E. Jentoft, and F. C. Jentoft, "Passivation Agents and Conditions for Mo_2C and W_2C: Effect on Catalytic Activity for Toluene Hydrogenation," *Journal of Catalysis* 347 (2017): 89–101, https://doi.org/10.1016/j.jcat.2017.01.002.

23. C. A. Schneider, W. S. Rasband, and K. W. Eliceiri, "NIH Image to ImageJ: 25 Years of Image Analysis," *Nature Methods* 9 (2012): 671–675, https://doi.org/10.1038/nmeth.2089.

24. O. Proux, V. Nassif, A. Prat, et al., "Feedback System of a Liquid-nitrogen-cooled Double-crystal Monochromator: Design and Performances," *Journal of Synchrotron Radiation* 13 (2006): 59–68, https://doi.org/10.1107/S0909049505037441.

25. A. Aguilar-Tapia, S. Ould-Chikh, E. Lahera, et al., "A New High Temperature Reactor for operando XAS: Application for the Dry Reforming of Methane Over Ni/ZrO_2 Catalyst," *Review of Scientific Instruments* 89 (2018): 035109, https://doi.org/10.1063/1.4998929.

26. G. Landrot and E. Fonda, "Fastosh: A Software for the Treatment of XAFS Datasets of Environmental Relevance or Acquired in Operando Conditions," *Journal of Synchrotron Radiation* 32 (2025): 1085–1094, https://doi.org/10.1107/S1600577525003923.

27. P. Liang, H. Gao, Z. Yao, et al., "Simple Synthesis of Ultrasmall β-Mo_2C and α-MoC_{1-x} Nanoparticles and New Insights Into Their Catalytic Mechanisms for Dry Reforming of Methane," *Catalysis Science & Technology* 7 (2017): 3312–3324, https://doi.org/10.1039/C7CY00708F.

28. Q. Rong, W. Ding, G. Liu, et al., "Insight Into the Key Factors of β-Mo_2C Catalyst for the Reverse Water Gas Shift Reaction," *RSC Advances* 2025, 15, 8346–8353.

29. P. Yin, H. Cai, X. Zhang, et al., "α-MoC_{1-x} Nanorods as an Efficient Hydrogen Evolution Reaction Electrocatalyst," *New Journal of Chemistry* 45 (2021): 10396–10401, https://doi.org/10.1039/D1NJ01088C.

30. N. S. Athanasiou, "Structural Instability and Superconductivity of the Defect Cubic Structure δ-MoC_{1-x}," *Modern Physics Letters B* 11 (1997): 939–947, https://doi.org/10.1142/S0217984997001158.

31. A. S. Kurlov and A. I. Gusev, "Phase Equilibria in the W–C System and Tungsten Carbides," *Russian Chemical Reviews* 75 (2006): 617–636, https://doi.org/10.1070/RC2006v075n07ABEH003606.

32. J. Zhu, E. A. Uslamin, N. Kosinov, and E. J. M. Hensen, "Tuning the Reactivity of Molybdenum (oxy)Carbide Catalysts by the Carburization Degree: CO_2 Reduction and Anisole Hydrodeoxygenation," *Catalysis Science & Technology* 10 (2020): 3635–3645, https://doi.org/10.1039/D0CY00484G.

33. G. Mühlbauer, G. Kremser, A. Bock, J. Weidow, and W.-D. Schubert, "Transition of W_2C to WC During Carburization of Tungsten Metal Powder," *International Journal of Refractory Metals and Hard Materials* 72 (2018): 141–148, https://doi.org/10.1016/j.ijrmhm.2017.12.018.

34. C. F. Holder and R. E. Schaak, "Tutorial on Powder X-ray Diffraction for Characterizing Nanoscale Materials," *ACS Nano* 13 (2019): 7359–7365, https://doi.org/10.1021/acsnano.9b05157.

35. B. Frank, Z.-L. Xie, K. F. Ortega, M. Scherzer, R. Schlögl, and A. Trunschke, "Modification of the Carbide Microstructure by N- and S-functionalization of the Support in Mo_xC/CNT Catalysts," *Catalysis Science & Technology* 6 (2016): 3468–3475, https://doi.org/10.1039/C5CY01480H.

36. A. Shrestha, X. Gao, J. C. Hicks, and C. Paolucci, "Nanoparticle Size Effects on Phase Stability for Molybdenum and Tungsten Carbides," *Chemistry of Materials* 33 (2021): 4606–4620, https://doi.org/10.1021/acs.chemmater.1c01120.

37. M. Arbib, E. Silberberg, F. Reniers, and C. Buess-Herman, "On the Synthesis and Characterization of Mixed (Mo,W) Carbides," *Journal of the European Ceramic Society* 18 (1998): 1503–1511, https://doi.org/10.1016/S0955-2219(98)00070-3.

38. D. Akmach, C.-C. Tran, T. Stevanovic, A. El Kadib, and S. Kaliaguine, "Eugenol Hydrodeoxygenation over Mixed Mo–W Carbides," *Chemsuschem* 17 (2024): e202301767, https://doi.org/10.1002/cssc.202301767.

39. F. de Groot, "High-Resolution X-ray Emission and X-ray Absorption Spectroscopy," *Chemical Reviews* 101 (2001): 1779–1808, https://doi.org/10.1021/cr9900681.

40. J. Timoshenko and B. R. Cuenya, "In Situ/Operando Electrocatalyst Characterization by X-ray Absorption Spectroscopy," *Chemical Reviews* 121 (2021): 882–961.

41. S. Bordiga, E. Groppo, G. Agostini, J. A. van Bokhoven, and C. Lamberti, "Reactivity of Surface Species in Heterogeneous Catalysts Probed by in Situ X-ray Absorption Techniques," *Chemical Reviews* 113 (2013): 1736–1850, https://doi.org/10.1021/cr2000898.

42. S. Britto, C. M. A. Parlett, S. Bartlett, J. D. Elliott, K. Ignatyev, and S. L. M. Schroeder, "Intermediates During the Nucleation of Platinum Nanoparticles by a Reaction With Ethylene Glycol: Operando X-ray Absorption Spectroscopy Studies With a Microfluidic Cell," *The Journal of Physical Chemistry C* 127 (2023): 8631–8639, https://doi.org/10.1021/acs.jpcc.2c08749.

43. C. A. Nunes, E. C. Resende, I. G. R. Aes, A. S. Anastácio, and M. C. Guerreiro, "In-situ Monitoring of the Structure of a Goethite-based Catalyst During Methane Oxidation by X-ray Absorption near-edge Structure (XANES) Spectroscopy Assisted by Chemometric Methods," *Applied Spectroscopy* 65 (2011): 692–697, https://doi.org/10.1366/10-06202.

44. W. H. Cassinelli, L. Martins, A. R. Passos, et al., "Multivariate Curve Resolution Analysis Applied to Time-resolved Synchrotron X-ray Absorption Spectroscopy Monitoring of the Activation of Copper Alumina Catalyst," *Catalysis Today* 229 (2014): 114–122, https://doi.org/10.1016/j.cattod.2013.10.077.

45. A. Iglesias-Juez, G. L. Chiarello, G. S. Patience, and M. O. Guerrero-Pérez, "Experimental methods in chemical engineering: X -ray absorption spectroscopy— XAS, XANES, EXAFS, XANES, EXAFS," *The Canadian Journal of Chemical Engineering* 100 (2022): 3–22, https://doi.org/10.1002/cjce.24291.

46. U. Jayarathne, P. Chandrasekaran, A. F. Greene, et al., "X-ray Absorption Spectroscopy Systematics at the Tungsten L-Edge," *Inorganic Chemistry* 53 (2014): 8230–8241, https://doi.org/10.1021/ic500256a.

47. G. Bunker, *Introduction to XAFS: A Practical Guide to X-ray Absorption Fine Structure Spectroscopy* (Cambridge University Press, 2010), https://doi.org/10.1017/CBO9780511809194.

48. G. Leclercq, M. Kamal, J. M. Giraudon, et al., "Study of the Preparation of Bulk Powder Tungsten Carbides by Temperature Programmed Reaction With CH_4+ H_2 Mixtures," *Journal of Catalysis* 158 (1996): 142–169, https://doi.org/10.1006/jcat.1996.0015.

49. A. Löfberg, A. Frennet, G. Leclercq, L. Leclercq, and J. M. Giraudon, "Mechanism of WO_3 Reduction and Carburization in CH_4/H_2 Mixtures Leading to Bulk Tungsten Carbide Powder Catalysts," *Journal of Catalysis* 189 (2000): 170–183, https://doi.org/10.1006/jcat.1999.2692.

50. D.-V. N. Vo and A. A. Adesina, "Kinetics of the Carbothermal Synthesis of Mo Carbide Catalyst Supported on Various Semiconductor Oxides," *Fuel Processing Technology* 92 (2011): 1249–1260, https://doi.org/10.1016/j.fuproc.2011.02.012.

51. S. Chaudhury, S. K. Mukerjee, V. N. Vaidya, and V. Venugopal, "Kinetics and mechanism of carbothermic reduction of MoO_3 to Mo_2C," *Journal of Alloys and Compounds* 261 (1997): 105–113, https://doi.org/10.1016/S0925-8388(97)00212-0.

52. B. Frank, K. Friedel, F. Girgsdies, X. Huang, R. Schlögl, and A. Trunschke, "CNT-Supported Mo x C Catalysts: Effect of Loading and Carburization Parameters," *Chemcatchem* 5 (2013): 2296–2305, https://doi.org/10.1002/cctc.201300010.

Supporting Information

Additional supporting information can be found online in the Supporting Information section.

Supporting File: cctc70616-sup-0001-SuppMat.docx.